Journal of Materials Chemistry A

ROYAL SOCIETY OF CHEMISTRY

PAPER

View Article Online
View Journal | View Issue

Cite this: J. Mater. Chem. A, 2025, 13, 40201

Design and prompt synthesis of a hydrazone-linked covalent organic framework with binding pockets for lanthanides: luminescent pH and ratiometric temperature sensing

Himanshi Bhambri † and Sanjay K. Mandal *

Focusing on the exceptional traits of the highly functionalized, flexible, and yet infrequent hydrazone linkages, a new covalent organic framework, namely **BTD**, is synthesized by a fast crystallization technique within 1.5 h. Extensive characterization by various spectroscopic and microscopic techniques, powder X-ray diffraction, and computational simulation confirms its purity, structural features, and porous nature. The framework is locked due to the presence of secondary interactions, such as intralayer (N···H–O and C–H···O=C) and interlayer (N–H···O) H-bonding as well as π–π stacking, which provide in-plane rigidness in the staggered AB-type stacking of layers. These strong interactions can be a possible reason for the prompt crystallization of **BTD**. The dual proton donor and acceptor sites offered by the functionalized hydrazone linkage in **BTD** lead to the wide-range, colorimetric, luminescent detection of hydrogen ion concentrations. Its luminescence is highest at pH 4 but quenched in a strong basic medium (pH 13). Furthermore, utilizing the characteristics of hydrazone connectivity and anchored functional groups (carbonyl and hydroxy), trivalent lanthanides are incorporated onto the decorated pockets, yielding **Tb@BTD** and **Eu@BTD**. Utilizing the remarkable thermal detection features of lanthanide-decorated COFs, ratiometric temperature detection studies were performed in aqueous and methanolic slurries. The computed relative sensitivity values for **Tb@BTD** and **Eu@BTD** are 1.404% K^{-1} and 1.118% K^{-1} at 333 K in water and 2.73% K^{-1} and 2.29% K^{-1} at 313 K in methanol, respectively. For demonstrating the utility of both COFs in real environmental conditions, the change in luminescence is studied in the temperature range of 308–320 K. With a quenching of 22%, **Eu@BTD** proves to be a better candidate for effective luminescent thermometric applications under physiological conditions.

Received 12th August 2025
Accepted 2nd October 2025

DOI: 10.1039/d5ta06543g

rsc.li/materials-a

Introduction

With the advancement in material synthesis, numerous organic polymers have been designed, manufactured, and successfully made workable by exploring their outstanding physical and chemical features.[1] Covalent organic frameworks (COFs) are one type of such materials that are well-known for their diverse functionalities, stability under drastic conditions, and long-range order.[2,3] However, attaining the three properties in a single organic polymer is a challenging and laborious task when flexibility is involved.[4–8] A majority of COFs utilize rigid building units and functional groups to maintain their structural integrity. For instance, boroxine, imine, triazine, azine, and phenazine linkages provide a single connectivity to the monomers, which go through multiple bond-making and breaking processes to ensure the orderly arrangement under thermodynamically controlled conditions. On the other hand, certain unique linkages like β-ketoenamine, bis(benzimidazole/oxazole), and thiazole go through a double-locking system to anchor the connection either by an irreversible reaction (like tautomerism) or cyclization.[3] The two cases mentioned above support the framework formation by monomers of limited flexibility. However, as far as flexible or semi-flexible linkages are concerned, the successful knitting of a crystalline, functional, and robust COF is difficult to achieve. The hydrazone linkage is one such flexible connectivity that is known to form robust COFs using its hydrogen-bond-forming capability.[9,10] On top of this, combining luminescent properties in such frameworks is another hurdle to pass.

In the past decade, fundamental principles have been established to learn about the factors responsible for the crystallinity of COFs. Conventional syntheses of crystalline COF requires: (a) proximate polarity of one or more solvents,[11,12] (b)

Department of Chemical Sciences, Indian Institute of Science Education and Research Mohali, Sector 81, Manauli PO, S.A.S. Nagar, Mohali, Punjab 140306, India. E-mail: sanjaymandal@iisermohali.ac.in

† Current address: Department of Education, School of Education, Central University of Punjab, Ghudda, Bathinda, Punjab 151401, India.

drastic temperature conditions of 120 °C or above,[3,9,13,14] (c) strictly inert or vacuum conditions throughout the reaction,[15] (d) prolonged reaction time of 3–9 days,[13] (e) harsh acids and bases as catalysts,[13,16,17] and (f) undisturbed environment.[3,15] On the other hand, interlayer hydrogen bonding and dipole-induced stacking also play a vital role in the attainment of periodicity in the framework. Lately, the importance of a double locking system for hydrazone-connected linkages has been emphasized, wherein interlayer and intralayer H-bonding help to build a properly stacked framework with remarkable chemical and water stability.[18–21] These systems are constructed under extreme conditions as mentioned above. In view of the above background and opportunities, we took on the challenge of reducing the extended reaction time and moderating the harsh reaction conditions to tailor a crystalline hydrazone-linked COF.[18]

In this contribution, we have synthesized a new hydrazone-linked COF, named **BTD**, using C_3-symmetric benzene-1,3,5-tricarbohydrazide (BTCONN) and C_2-symmetric 4,4′-dihydroxy-(1,1′-biphenyl)-3,3′-dicarbaldehyde (DPDC) monomers *via* sonication followed by heating at 120 °C under an aerobic environment for 1.5 hours. A crucial step in this work is the selection of monomers prioritizing rich functionalities, such as proton-donor and scavenging sites. The monomer BTCONN incorporates flexible functional units, *i.e.*, carbohydrazide (CO–NH–NH_2), that facilitate a highly flexible connectivity with dialdehyde units in DPDC (Scheme 1). The additional functionalities, such as the hydroxy groups in DPDC and the carbonyl groups of BTCONN (marked by a star symbol in Scheme 1), are positioned in such a way that a binding pocket is formed in the skeleton for entrapping metal ions *via* a post-synthetic modification. Furthermore, the biphenyl unit in DPDC adds to the flexibility of the framework by allowing molecular rotation through the C–C bond, which further raises the challenge to attain long-range order in the material.

Temperature and hydrogen ion concentration are two vital parameters that require a great deal of care in biological systems and living environments.[22,23] In recent decades, thermometry has gained considerable attention as we have moved from traditional, non-invasive contact thermometers to contactless ones.[24] In furtherance of this progress, precise quantification of thermal emissivity is critically important and can be attained with sufficiently sensitive sensors.[25] Presently, many sophisticated thermometry techniques have been developed and practiced for high-accuracy temperature measurements. Luminescence thermometry has become one of the most widely used methods because it can measure temperature-based changes in wavelength, intensity, lifetime, or the ratio of different signals. The ratiometric luminescent sensing technique, which utilizes Boltzmann's law for thermalization with prompt readouts, is simple to use and provides a self-calibration approach to thermal detection.[26] The other indispensable variable – the potency of hydrogen – contributes greatly in many fields, such as determining the susceptibility of reactions, drug delivery and other medical diagnoses, in addition to monitoring water quality, *etc.* The ability of luminescence-based calorimetric sensors to selectively detect and interact with protons in aqueous media provides a practical approach for this study.[9,27,28]

The strategic use of highly functionalized hydrazone-linked **BTD** was employed to boost its colorimetric, luminescent, H^+ donating, and scavenging properties in acidic as well as alkaline media. Moreover, the linkages generate pockets decorated with heteroatoms for trapping metal ions *via* chelation (Scheme 1). To exhibit luminescent thermometric properties, **Tb@BTD** and **Eu@BTD** COFs were formed by post-synthetic modification of **BTD** *via* the insertion of Tb^{3+} and Eu^{3+}, respectively. Both frameworks were subjected to a micro temperature range (258 to 333 K) to record the effect on luminescence in polar protic media.

Experimental section

Materials and methods

For material synthesis and applications, all the required chemicals and solvents were received from standard commercial sources and used as such without further processing. BTCONN and DPDC were synthesized using the reported procedures.[29,30]

Synthesis of BTD

A mixture of BTCONN (30 mg, 0.12 mmol) and DPDC (43.6 mg, 0.18 mmol) was prepared in 5 mL mesitylene/dioxane (1 : 1)

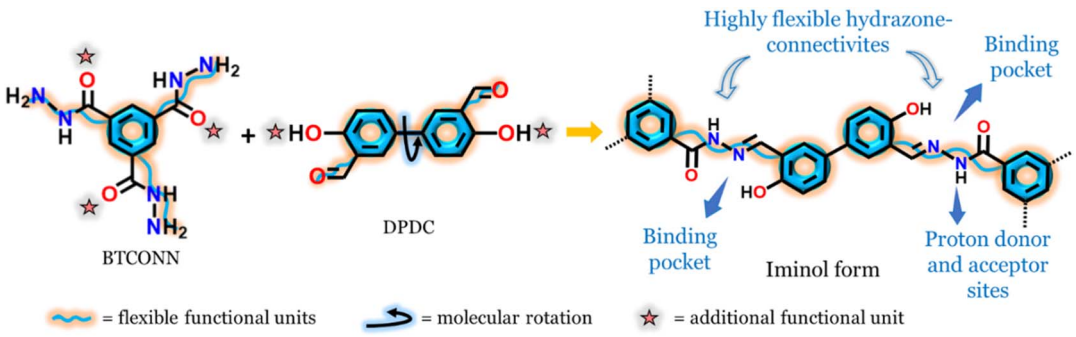

Scheme 1 Illustration of the functionalities of monomers used for constructing hydrazone-linked COFs with metal binding pockets, and the proton donor and scavenger properties.

taken in a 15 mL glass vial. To it, 250 μL of 6 M acetic acid was added as a catalyst. The reaction mixture was sonicated for 30 minutes and transferred to a 10 mL round-bottom flask, which was then refluxed at 120 °C for 1 h under an aerobic environment. The resultant bright-yellow precipitate was filtered and washed well with acetone, tetrahydrofuran, dimethylacetamide and methanol. The dried precipitate was used for further characterization. Yield: 40 mg (88%). ^{13}C ssNMR (CPMAS, 400 MHz): 160.31, 156.02, 151.18, 130.17, 116.74. Selected FT-IR peaks (KBr pellets, cm^{-1}): 3413 (m), 3272 (s), 3050 (m), 1655 (s), 1615 (s), 1593 (s), 1524 (m), 1318 (m), 1273 (m), 1016 (m), 732 (w), 691 (w), 584 (w).

Synthesis of Ln@BTD

In a 25 mL round-bottomed flask, 30 mg (0.025 mmol) of **BTD** was mixed with 21.8 mg (0.05 mmol) $Tb(NO_3)_3 \cdot 5H_2O$ or 21.4 mg (0.05 mmol) $Eu(NO_3)_3 \cdot 5H_2O$ in 10 mL acetonitrile. The mixture was stirred under reflux conditions for 24 h. The color of the material turned dark brown over time. The lanthanide-induced frameworks, namely **Tb@BTD** and **Eu@BTD**, were cooled, filtered, washed multiple times with water and acetonitrile, and air-dried. Selected FT-IR peaks (KBr pellets, cm^{-1}): 3167 (m), 3040 (m), 1673 (s), 1620 (s), 1555 (s), 1383 (s), 1265 (m), 738 (w) for **Tb@BTD**; 3199 (m), 3040 (m), 1665 (s), 1624 (s), 1555 (s), 1383 (s), 1269 (m), 734 (w) for **Eu@BTD**.

Pre-treatment of BTD and Ln@BTD

All three frameworks, namely **BTD**, **Tb@BTD** and **Eu@BTD**, were pretreated for 10 h at 100 °C under high vacuum to remove moisture and solvents used for washing, before use in sensing studies.

Procedure for sensing studies

The luminescence spectra of **BTD** were recorded in a slurry mode with suspensions prepared with 0.5 mg of sample in 1 mL of solvent.

Proton donor and scavenger test. A homogeneous suspension of **BTD** was made in double-distilled water of ultrahigh purity (18.2 MΩ cm@25 °C) with varying H^+ concentrations. The chosen pH values were in the acidic, neutral, and basic range, *i.e.*, 0, 2, 4, 6, 7, 10, 12, 13. After 30 minutes of sonication, the slurry was irradiated at 390 nm, and the emission was recorded in the range of 500–730 nm.

Temperature sensing. A homogeneous slurry of **Tb@BTD** and **Eu@BTD** was made in polar protic solvents, *i.e.*, water and methanol, and well suspended by sonicating for 30 minutes. The effect of temperature on the luminescence of **Tb@BTD** and **Eu@BTD** was studied in water from 278 to 333 K and in methanol from 258 to 313 K. For thermal sensing under physiological conditions, luminescence in the narrow temperature range of 308 to 320 K was checked. In each case, the slurry was irradiated at 380 nm, and the emission was recorded in the range of 430–730 nm.

Results and discussion

Synthesis and structure solution

The synthesis of **BTD** involved a combination of a C_3-symmetric trihydrazide, BTCONN, and a C_2-symmetric linear dialdehyde, DPDC. These reaction components were first synthesized in good yield and well characterized using NMR and FT-IR spectroscopic analyses (Fig. S1–S4). A mixture of BTCONN and DPDC (1 : 1.5 ratio) taken in a vial was sonicated well in the presence of mesitylene/dioxane/6 M acetic acid for 30 minutes. With brightening of the pale-yellow color of the mixture, it was then refluxed for an hour to yield a bright-yellow material in 88% yield (Fig. 1a). Furthermore, the functionality was tailored with the carbohydrazide and hydroxy-substituted carbaldehyde to provide a suitable pocket in the **BTD** for metal incorporation. Both **Tb@BTD** and **Eu@BTD** were synthesized by combining **BTD** with $Tb(NO_3)_3 \cdot 5H_2O$ and $Eu(NO_3)_3 \cdot 5H_2O$, respectively, under reflux conditions for 24 h. The bright-yellow colour of the **BTD** turned dark brown after metal ion binding (Fig. 1a).

BTD consists of flexible hydrazone linkages that connect the monomers in a periodic fashion. The –CO–NH–NH_2 functionality of BTCONN forms an imine bond with the –CHO groups in the DPDC monomer, resulting in the iminol form of **BTD** (Fig. 1a). The use of highly flexible functional groups and a rotatable biphenyl core poses a challenge to attain long-range order in **BTD**, which is accomplished by locking the skeletal framework by hydrogen-bonding. An essential factor in this is the –NH, –C–OH, and –C═O functionalities, which help in building large-sized crystallites due to the formation of interlayer and intralayer hydrogen bonds, leading to rapid crystallization. The WAXS pattern for **BTD** showcased well-defined diffraction peaks, which were further compared with those of the monomers to establish its phase purity, free from the monomers (Fig. S5).

To learn about the connectivity and structure of **BTD**, a comprehensive crystallographic examination was conducted using the BIOVIA Materials Studio 21.1.[31] The framework was successfully optimized through simulations with the DFTB+ module and found to be present in the *P*6 space group of the hexagonal lattice system with lattice parameters $a = b = 35.762$ Å, $c = 3.553$ Å, $\alpha = \beta = 90°$, $\gamma = 120°$ (Table S1). The diffraction peaks for the optimized structure appeared at $2\theta = 2.8°$, 4.9°, 5.7°, 7.5°, 8.5°, 11.4°, 14.28°, 17.1°, 18.7°, 19.8°, 21.6°, 22.9°, 26.5°, 29.9° and 33.8°, corresponding to (100), (110), (200), (210), (300), (400), (500), (600), (610), (440), (710), (800), (301), (660) and (541), respectively, with *d*-values of 30.9, 17.8, 15.5, 11.7, 10.3, 7.7, 6.2, 4.7, 4.4, 4.1, 3.8, 3.3, 2.98, 2.6 Å, respectively, using Bragg's equation ($n\lambda = 2d \sin\theta$, where $n = 1$ and $\lambda = 1.54$ Å). A slight broadening of the peaks is also observed due to the highly flexible connectivities.[9] The simulated WAX pattern of **BTD** was refined with eclipsed (AA) and staggered (AB or ABC) structures, and found to be the best fit for AB stacking with $R_p = 6.7\%$ and $R_{wp} = 14.2\%$ (Fig. 1b). The structure was locked with the secondary interactions, such as intra- and inter-layer H-bonding and π–π stacking. The intralayer H-bonding between N···H–O and C–H···O═C groups (2.4–2.0 Å) restricts

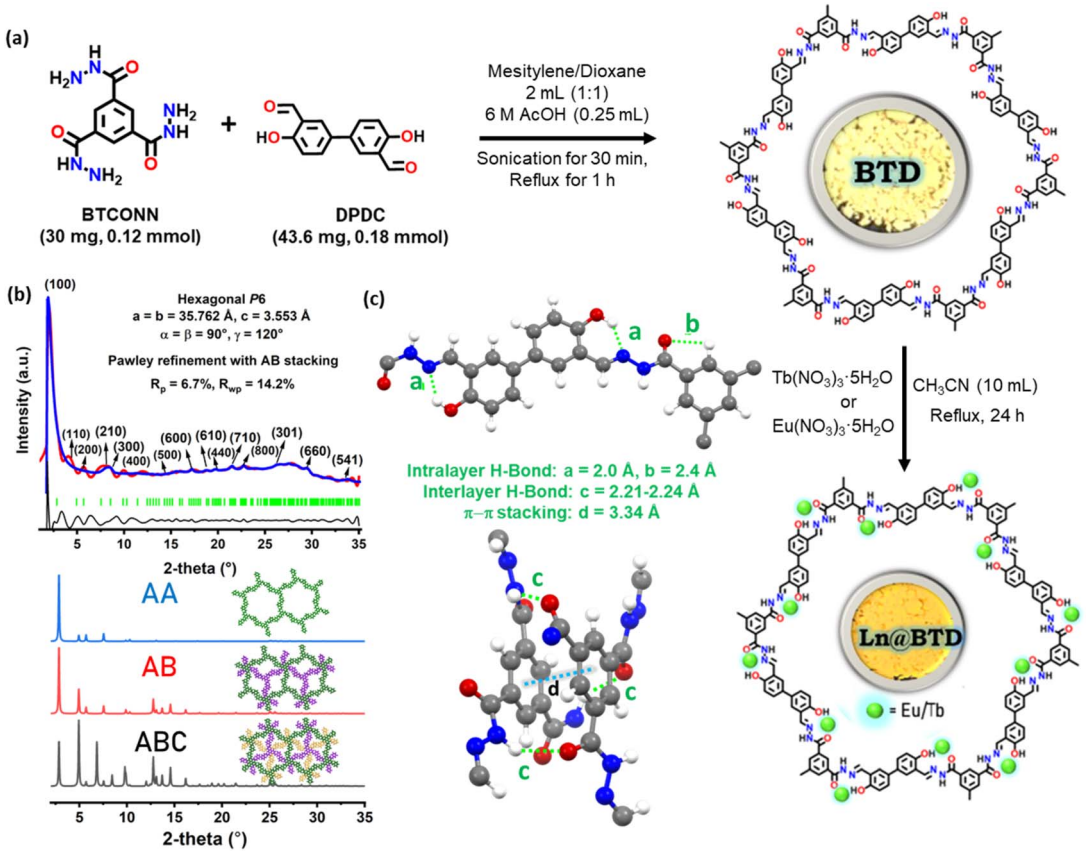

Fig. 1 (a) Synthesis of **BTD** and **Ln@BTD** with corresponding photographs shown in the insets; (b) X-ray diffractograms showing experimental (blue) and Pawley refinement (red), with the difference plot (black) and Bragg peak positions (green) overlaid with simulated diffraction patterns of **BTD** in AA, AB, and ABC stacking modes; (c) illustration of intra- and inter-layer hydrogen bonding within the **BTD** framework. The geometry-optimized structure was obtained using the DFTB+ module in BIOVIA Materials Studio 21.1.[31]

intramolecular rotations to gain in-plane rigidity among the layers. On the other hand, the stacking of layers in **BTD** is supported by interlayer H-bonding between N–H···O groups (2.21–2.24 Å) and π–π stacking of the phenyl rings (3.34 Å). The interlayer and intralayer H-bond distances are given in Fig. 1c. A broad hump in the 25–28° range is indicative of a fine stacking of the 2D layers.[32] These strong interactions can be a possible reason for the prompt crystallization of **BTD**, eliminating the time-consuming solvothermal method for the bond-making and breaking processes.

Spectroscopic and microscopic characterization

In order to provide further confirmation of the synthesis of **BTD**, its FTIR spectrum and XRD profile were compared with those of BTCONN and DPDC. There is a complete disappearance of peaks around 3291 and 3186 cm^{-1} for the primary amine moiety in BTCONN, which confirms the formation of hydrazone linkages (Fig. S6). Moreover, the peak at 3272 cm^{-1} persisted in both BTCONN and **BTD** due to the secondary amine group. Sharp peaks that appeared at 3050, 1615 and 1273 cm^{-1} show the presence of aromatic C–H, C=C and C–N in **BTD**, respectively. Moreover, the C=O stretching frequency for the NH–C=O moiety is observed at 1655 cm^{-1}. A sharp peak that appeared at 1592 cm^{-1} indicates imine bond formation, and the broad hump above 3400 cm^{-1} shows the presence of hydroxy groups in the polymer.[32] Furthermore, the FTIR spectra of **Tb@BTD** and **Eu@BTD** show peaks for the N–C–O, C–N and C=C stretches with the disappearance of a peak for the N–H stretch (Fig. S7). An additional peak for the N–O stretching for the coordinated nitrate group is also observed around 1383 cm^{-1}, respectively, in both **Tb@BTD** and **Eu@BTD**.

BTD exhibits high thermal stability up to 310 °C, as determined by thermogravimetric analysis (Fig. S8). However, this thermal resistance is maintained up to 250 °C following the incorporation of lanthanide ions into the framework (Fig. S9). The ^{13}C solid-state CP/MAS NMR spectrum of **BTD** displays a characteristic peak at 151.18 ppm corresponding to the carbon atom in the –C=N– hydrazone linkage formed between the BTCONN and DPDC monomers (Fig. S10). Additional signals at 160.3 ppm and 156 ppm are attributed to the carbon atoms of the C=O and C–OH groups, respectively. Notably, the crystallinity of **BTD** is preserved even after lanthanide incorporation, as evidenced by the diffraction pattern (Fig. S11).

The surface morphology of **BTD**, as observed through microscopic analysis, reveals a microrod-shaped structure (Fig. S12). The rod-like form of **BTD** remained stable even after the incorporation of lanthanides at its binding sites. The rods in

BTD, **Tb@BTD**, and **Eu@BTD** range in length from 0.4 to 1.3 μm. Crystallinity is evident in the selected area electron diffraction (SAED) patterns (Fig. 2a–f). Energy-dispersive X-ray (EDX) analysis and elemental mapping confirm the presence of all the expected elements in **Tb@BTD** and **Eu@BTD**, with atomic percentages of 1.24% Tb and 0.29% Eu, respectively (Fig. 2g–j).

The porosity and surface area of **BTD** and **Ln@BTD** were evaluated using nitrogen adsorption–desorption measurements at 77 K, applying the Brunauer–Emmett–Teller (BET) model. As shown in Fig. S13, **BTD** exhibited a type IV isotherm with an H3-type hysteresis loop, indicative of mesoporous characteristics and multilayer adsorption following monolayer completion. The BET surface area, calculated by fitting the data within the relative pressure (P/P_0) range of 0.05–0.25,[33–35] was 147 $m^2\ g^{-1}$ for **BTD**. In contrast, the surface areas for **Tb@BTD** and **Eu@BTD** were significantly reduced to 49.5 and 50.4 $m^2\ g^{-1}$, respectively (Fig. S14).[36] The observed H3 hysteresis loop suggests the presence of open-ended pores. The total pore volume decreased from 0.581 $cm^3\ g^{-1}$ in **BTD** to 0.34 $cm^3\ g^{-1}$ in **Ln@BTD**. This reduction in surface area and pore volume is likely attributed to the incorporation of Tb^{3+} and Eu^{3+} ions into the binding sites within the framework structure. The relatively low surface area can be attributed to its mesoporous structure and limited crystallinity, consistent with previous reports on various hydrazone-linked COFs, such as $HCOF_n$ (n = 1–4) (3–9 $m^2\ g^{-1}$),[37] Th-Bta and NH_2–Th-Bta (10 and 22 $m^2\ g^{-1}$, respectively),[38] TpBth and TaBth (54.26 and 20.12 $m^2\ g^{-1}$,

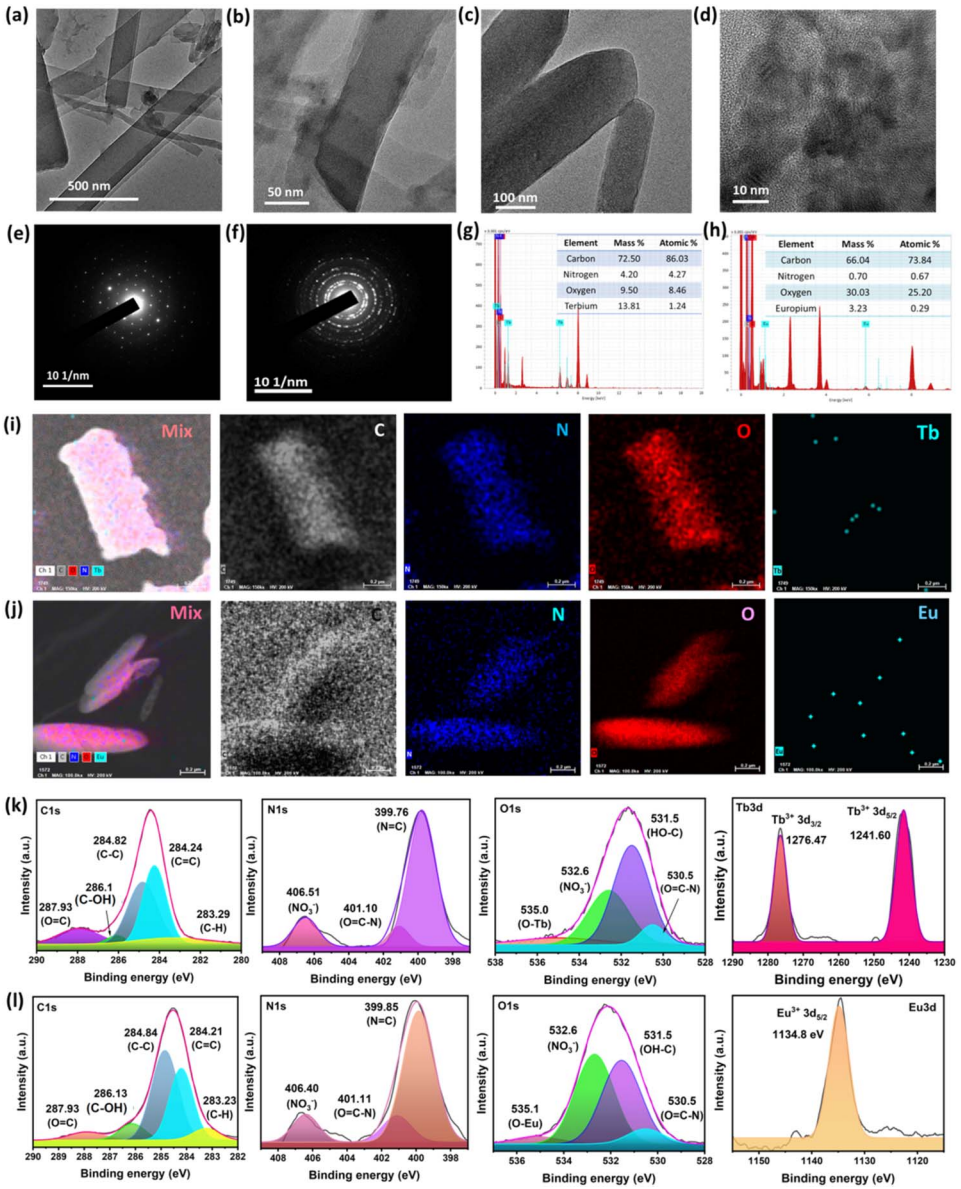

Fig. 2 TEM and HRTEM images of (a and b) **Tb@BTD** and (c and d) **Eu@BTD** with their SAED patterns in (e) and (f), respectively; (g and h) their respective EDX spectra and quantification in the inset along with elemental mapping (i) and (j), respectively; XPS profiles of individual elements for **Tb@BTD** in (k) and for **Eu@BTD** in (l).

respectively),[39] and $COF_{BMTH-TBT}$ and $COF_{BMTH-TFB}$ (39 and 114 $m^2\ g^{-1}$, respectively).[40] The pore size distribution (PSD) was analyzed using the nonlocal density functional theory (NLDFT) equilibrium model, revealing a primary pore size of 2.7 nm (Fig. S13b), which closely aligns with the simulated AB stacked structure (2.1 nm) as shown in the inset of Fig. S13a.

Additionally, the XPS analysis of **BTD** showcases deconvoluted peaks at 287.9 (C═O), 285.8 (C–OH), 285.1 (C–C), 284.3 (C═C) and 283.3 (C–H) eV for C 1s, 401.54 (O═C–N) and 400.24 (N═C) eV for N 1s, and 532.5 (C–OH) and 531.3 (N–C═O) eV for O 1s (Fig. S15). The atomic percentage obtained from the XPS analysis reveals 15.91% N, 15.96% O, and 68.12% C in **BTD** (Table S2). Information on the Ln-sites was also gained using XPS analysis of each **Ln@BTD**. The full spectra show the peaks corresponding to all elements present in the framework, *i.e.*, Tb/Eu, N, C and O. For **Tb@BTD**, the Tb 3d spectrum reveals binding energies at 1276.47 and 1241.6 eV associated with Tb $3d_{3/2}$ and Tb $3d_{5/2}$ in the trivalent state, respectively (Fig. 2k). After incorporation of Tb into **BTD**, there is a change in electron density of the N/O-atoms present in the hydrazone linkage, showing a slight shift in the deconvoluted peaks.[41] From the N 1s spectra, it is inferred that peaks at 401.1 and 399.76 eV are ascribed to the –NH– group for O═C–N and the imine nitrogen (N═C), respectively. An additional peak deconvoluted at 406.51 eV indicates the presence of NO_3^- on the terbium center. Furthermore, the corresponding peak for the NO_3^- group in the O 1s spectrum at 532.6 eV is also observed. Thus, it can be confirmed that Tb is bound to a deprotonated hydrazide nitrogen from the linkage, with a deprotonated phenoxy oxygen and one nitro group that balances its charge. A peak at 535 eV for the O–Tb interaction is distinctively seen, whereas no such peak is noted in the O 1s spectrum of **BTD**. Two additional peaks in the O 1s XPS spectra are observed for C–OH and O═C–N units at 531.5 and 530.5 eV. By deconvoluting the C 1s spectra of **Tb@BTD**, five peaks were observed at 287.93, 286.1, 284.82, 284.24 and 283.29 eV corresponding to C═O, C–OH, C–C, C═C and C–H carbons, respectively. The atomic % elucidated from the XPS analysis of **Tb@BTD** is 0.97% Tb, which is close to the value obtained from the EDX analysis (Table S2).

Similarly, the deconvoluted peaks for C 1s, N 1s and O 1s in **Eu@BTD** showed minor shifts compared to those in the XPS spectrum of **BTD** (*vide supra*). The Eu 3d spectrum shows a peak at 1134.8 eV for Eu^{3+} $3d_{5/2}$ (Fig. 2l). The N 1s and O 1s spectra revealed the presence of the nitro group with respective binding energies of 406.4 and 532.6 eV. Hence, the binding environment for Eu in **Eu@BTD** is similar to that for Tb. Moreover, the peaks for the amine nitrogen in the N 1s spectrum are observed at 401.11 and 399.85 eV for the two types of nitrogens, *i.e.*, O═C–N and imine (N═C), respectively. In the O 1s spectrum, the deconvoluted peaks at 531.5 and 530.5 eV are found for two types of oxygen, C–OH and O═C–N, respectively. An additional peak at 535.1 eV for the O–Eu band further confirmed the binding of Eu metal to **BTD**. The C 1s XPS spectrum included peaks at 287.93, 286.13, 284.84, 284.21 and 283.23 eV, ascribed to carbon atoms of C═O, C–OH, C–C, C═C and C–H carbons, respectively. The atomic % of Eu in the framework obtained from XPS analysis was 0.28%, which matches well with the quantification results from the EDX analysis (Table S2).

Optical properties

BTD is a bright-yellow luminescent active material with flexible hydrazone linkages. A preliminary test was conducted to check its emission. Placing 10 mg of **BTD** in the dark, the sample was then illuminated with a short-range UV light (365 nm). A glaring orange emission indicated its strong emission properties and was ascribed to an extended conjugation in the network (Fig. 3a). In a similar way, after binding of Ln^{3+} ions to the **BTD**, both the frameworks emit a deep-red color, which can be clearly seen under short-range UV light (Fig. 3a). From the Commission Internationale de l'Eclairage (CIE) chromaticity diagram, the coordinates of the spots were obtained at (0.53, 0.47) for **BTD**, (0.51, 0.39) for **Tb@BTD** and (0.56, 0.44) for **Eu@BTD**, which represent the orange and red regions in the color model (Fig. 3b).

Detailed information on the optical properties of the samples was gained from solid-state UV-vis diffuse reflectance spectroscopy (DRS) and luminescence studies. The absorption spectrum of **BTD** showed a maximum in the range of 390–420 nm (Fig. S15). Similarly, the lanthanide-induced frameworks, *viz.* **Tb@BTD** and **Eu@BTD**, were studied to compare their optical properties with those of **BTD**. The solid-state UV-vis DRS spectra showed a broader excitation range for **Ln@BTD** at higher wavelengths, *i.e.*, 380–500 nm. This was ascribed to the absorption corresponding to $\pi \rightarrow \pi^*$ and/or $n \rightarrow \pi^*$ transition for the aromatic ring and heteroatoms, Tb^{3+} ($^7F_6 \rightarrow {}^5D_{1-4}$) and Eu^{3+} ($^7F_0 \rightarrow {}^5D_{0-2}$) in **Ln@BTD** (Fig. S16).[26]

Furthermore, the solid-state fluorescence studies were conducted in which **BTD** and its lanthanide-induced derivatives were irradiated at a wavelength range of 390–420 nm. The emission spectra are shown in Fig. S17a with the emission maxima in the visible region of 500–700 nm. The emission maxima were found at 584 nm (for **BTD**) and 574 and 626 nm (for **Tb@BTD**, $^5D_4 \rightarrow {}^7F_{0-6}$ and **Eu@BTD**, $^5D_0 \rightarrow {}^7F_{0-6}$, respectively). Such emission at high wavelength indicates emission of a deep color in the orange-red region (inset of Fig. S17a). An additional fluorescence study was conducted when the monomers of **BTD**, *i.e.*, BTCONN and DPDC, were excited at 380 nm and their emission was recorded in the 500–700 nm range. It is noteworthy that no evident emission is observed in either case (Fig. S17b), which further confirms the formation of **BTD** in pure form.

Utilizing such properties, **BTD** was exploited for in-depth pH-dependent luminescence studies, while the Ln-induced frameworks were used for the ratiometric temperature detection in protic solvents of varying polarity (*vide infra*).

Proton donor and scavenger tests with BTD

The functionalized hydrazone linkages contain free C═O, –OH and –NH groups that facilitate proton removal and abstraction under different H^+ ion concentrations. On this account, **BTD** fulfils the candidature for a pH-responsive proton donor and scavenger test. Before testing it for the proton donor and

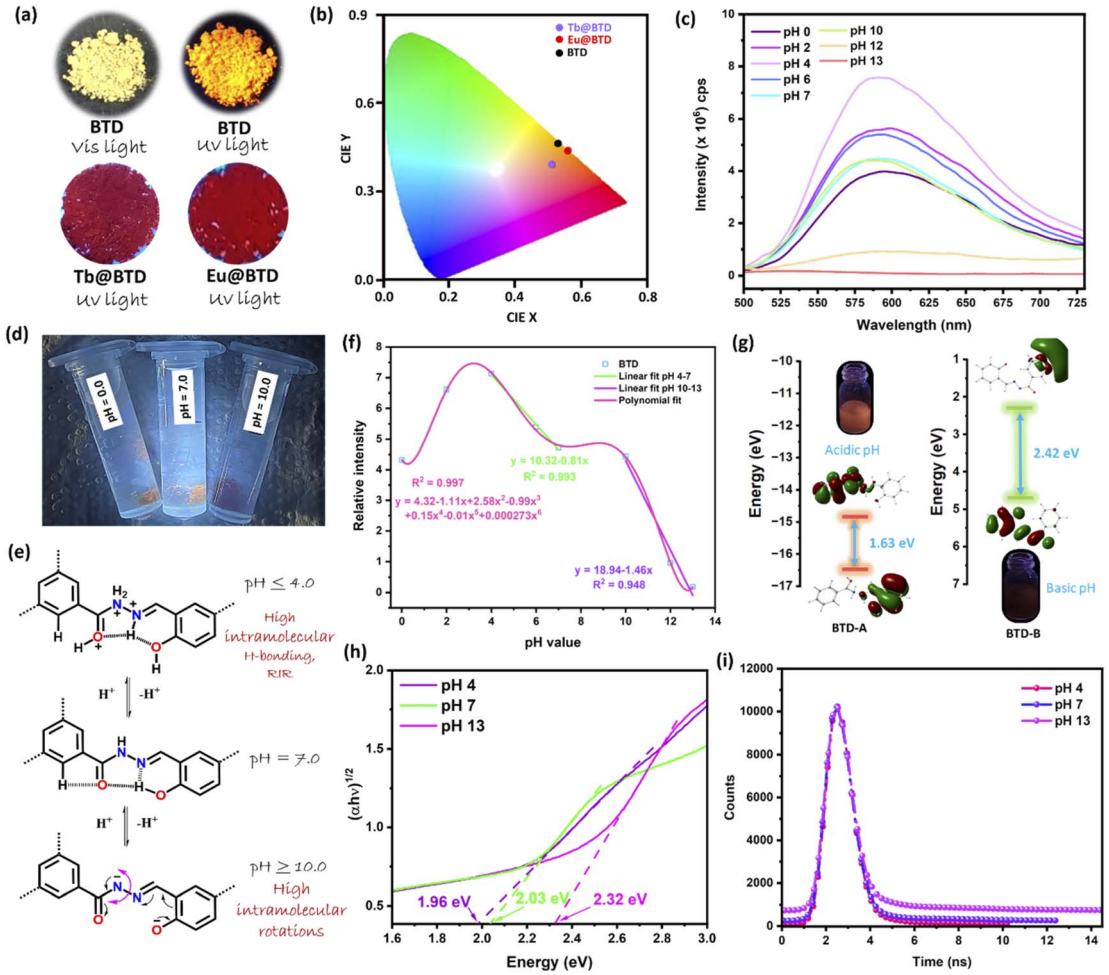

Fig. 3 (a) Digital photographs under visible and UV light, and (b) chromaticity diagram for **BTD**, **Tb@BTD** and **Eu@BTD**; (c) luminescence spectra showing the effect of H^+ ion concentration on the luminescence intensity of **BTD**; (d) digital images of **BTD** at acidic (pH = 0), neutral (pH = 7) and basic (pH = 10) environments; (e) mechanism showing the effect of pH on luminescence; (f) linear and polynomial fit for H^+ detection in varying pH range; (g) energy optimized HOMO–LUMO orbitals of protonated and deprotonated **BTD**, namely, **BTD-A** and **BTD-B**, respectively, using DFT calculations, along with the images of their cuvettes, (h) band gap calculated from the Tauc plot; and (i) time-resolved lifetime decay profile of **BTD** at pH = 4, 7 and 13.

scavenger test, 3 mg of **BTD** was soaked in 2 mL aqueous solution of pH 4, 7 and 13 for 2 days to examine its integrity under both strong acidic and basic conditions. Interestingly, the crystalline nature of **BTD** was retained in this pH range (Fig. S18). This prompted us to conduct sensing experiments with **BTD** in an aqueous slurry medium.

To monitor the proton-donating and scavenging tendency by noting the effect of hydrogen potency on the luminescence intensity of **BTD**, its homogeneous suspension was prepared in varying pH solutions, *i.e.*, pH 0, 2, 4, 6, 7, 10, 12 and 13 to record the emission spectra. A fairly high luminescence emission in the range of 7.5×10^6 cps was observed at pH 4. However, a slight quenching in the emission signal was noted at pH < 4. On the other hand, at pH 7, the emission intensity was slightly less and then drastically decreased until basic pH 13 was attained (Fig. 3c). The digital images of **BTD** in pH 0, 7 and 10 under UV light showed illumination in acidic as well as neutral media, while quenching behavior was observed beyond pH 10 (Fig. 3d). In addition to this, there is a slight change in the emission maxima (λ_{em}) of **BTD** with the variation in pH. From Fig. 3b, it was noted that the λ_{em} value at pH 7 is 592 nm. In acidic medium, the emission maximum was redshifted by ~6 nm. Whereas, when the pH was increased to 10, the λ_{em} was lowered by 4 nm. At pH 13, no λ_{em} was observed due to the complete quenching of the luminescence intensity of **BTD**.

A possible explanation for the varying PL response of the framework in different pH media is ascribed to the multiple electrostatic interactions prevailing within the system. At pH 4, an adequate amount of protonation of –NH and –C=O groups restricts intramolecular rotations (RIR) and limits flexibility, due to which the energy dissipation ceases. This results in high luminescence with λ_{em} = 600 nm in a fairly acidic medium. Moreover, upon further increasing the acidic environment to pH 0, all the heteroatoms were fully protonated, leaving a positive charge on the framework, which was balanced by chloride (from the acid) and/or hydroxide (from the aqueous medium)

anions. We suspect that the electronic interactions at this stage lead to a slight decrease in the luminescence of **BTD**. Furthermore, in moving toward basic pH, in the range 6 to 10, the emission intensity was quenched slightly and then drastically until pH 13. This was attributed to the fact that there are rapid intramolecular rotations occurring in the flexible hydrazone linkages caused by the complete deprotonation of heteroatoms (Fig. 3e and f). Such rapid rotations lead to the dissipation of absorbed energy in a non-radiative fashion, further leading to a complete quenching of the characteristic emission peak of **BTD** at $\lambda_{em} = 592$ nm.

To shed light on the mechanistic details of pH sensing studies, density functional theory (DFT) was implemented on the **BTD** core.[42] For this, the smallest unit of **BTD** was taken in two forms, *i.e.*, one with full protonation of all heteroatoms in the hydrazone linkage, and another with its complete deprotonation, mimicking acidic and basic pH environments, respectively. These units are labelled as **BTD-A** and **BTD-B**. The calculations showed a HOMO–LUMO gap of 1.63 eV in **BTD-A**. However, the corresponding gap in **BTD-B** was increased to 2.42 eV (Fig. 3g). The lower energy gap under acidic pH favours the higher luminescence in **BTD**, whereas it quenches when the energy gap increases under basic pH conditions. The band gap values obtained from the DFT calculations were further tallied with the experimental band gaps (E_g) obtained from the solid-state UV-vis DRS spectra of **BTD** at different pH (Fig. S19). The E_g values obtained from the Tauc plot ($(\alpha h\nu)^{1/2}$ *vs.* energy) are 1.96 eV, 2.03 eV and 2.32 eV for pH 4, 7 and 13, respectively (Fig. 3h). These band gap values further prove the strong emissive nature of **BTD** in acidic medium, attributed to its lower band gap value, and its weak emissive nature in basic medium, attributed to its corresponding higher band gap value.

Reversibility, reusability and stability tests. In order to prove the reversible nature of **BTD** toward proton donating and scavenging ability, its luminescence was recorded at pH 4, 7 and 13 up to five consecutive cycles. It was found that, in each cycle, the luminescence intensity nearly recovered to the value of the first cycle (Fig. S20). The intriguing aspect lies in the observable luminescent switching of **BTD**. This can be detected by the naked eye through ten cycles under visible light and for six cycles under UV light in the pH range of 4–13, as evidenced in the accompanying videos (Videos S1 and S2). The structural integrity of the sensor was retained after five cycles, indicating the reusability and stability of the framework (Fig. S21). Further support to the mechanistic insights of pH sensing was provided by the time-resolved lifetime measurements. The decay profiles of **BTD** at different pH values (Fig. 3i) were exponentially fitted with a good χ^2 value (1–1.14) and the average lifetime of **BTD** was found to be 0.013 ns (pH 4), 0.139 ns (pH 7) and 0.066 ns (pH 13). The emission lifetimes at neutral and basic pH are longer than that at acidic pH, which follows a dynamic quenching pathway during protonation and deprotonation of the heteroatoms present in the framework. Furthermore, the exponential decay constants were calculated in each of the above-mentioned cases. The values as obtained by reciprocating the lifetime decays are 77 ns^{-1} at pH 4, 7.2 ns^{-1} at pH 7, and 15.2 ns^{-1} at pH 13.[43]

BTD is a rare example of a proton donor as well as a scavenging material that operates over a wide pH range, from pH 0 to 13. The trend is comparable to CONNCO, reported by our group, where significant increases and decreases in the luminescence intensity were noted with an increase in pH.[9] However, a few other examples, such as COF-JLU4, COF-HQ, and TPE-Por, have been reported as proton scavengers in various pH regions.[27,28,44–46] Additionally, the polynomial for **BTD** was fitted in the full pH range with an R^2 value of 0.997. For the quantitative study, the linear fit in the pH range above 4 was carried out using equations: $y = 10.32–0.81x$ for pH 4 to 7, and $y = 18.94–1.46x$ for pH 7 to 13 (Fig. 3f).

Temperature sensing by Ln@BTD

Changing the luminescence properties with a variation in temperature is a key feature for which trivalent lanthanide ions are well-known. The hydrazone linkages of **BTD** are highly functional and provide suitable chelating sites to bind Ln^{3+} ions efficiently. Incorporation of such ions on the polymer tends to enhance its emission spectrum with a shift from the ultraviolet region to the visible and near-infrared regions. Therefore, the two Ln-induced frameworks, *viz.* **Tb@BTD** and **Eu@BTD**, were utilized for ratiometric temperature sensing because of their sharp line-like peaks in the high-wavelength range.

Homogeneous suspensions of **Tb@BTD** and **Eu@BTD** frameworks were made in two different high-purity solvents, *i.e.*, double-distilled water and HPLC-grade methanol, to record their emission spectra in a wide temperature range of 278 to 333 K (for aqueous slurry), and 258 to 313 K (for methanolic slurry) after excitation at 380 nm. For **Tb@BTD** in aqueous medium, three peaks were observed at 298 K in the emission spectra. These include two small peaks at 436 and 724 nm for $^5D_3 \rightarrow {}^7F_4$ and $^5D_4 \rightarrow {}^7F_{0,2}$ bands of Tb^{3+}, respectively, and a broad peak in the range of 530–680 nm for the $^5D_4 \rightarrow {}^7F_{3–5}$ band of Tb^{3+} and $\pi^* \rightarrow \pi$ and/or $\pi \rightarrow$ n transition of **BTD** (Fig. S22).[47] It must be noted that the emission peak at 436 nm is merged with the Raman scattering peak for water molecules when excited at 380 nm.[48] The slurry was then slowly subjected to different temperatures ranging from 278 to 333 K, and the emission spectra were quenched with an increase in temperature (Fig. 4a). In this case, the maxima at 621 nm (for **BTD**) and 724 nm (for Tb^{3+}) were used to calculate the thermal sensitivity of the sensor (*vide infra*). On the other hand, the emission peaks recorded in the methanolic medium at 298 K showed a slight blueshift and appeared at 428 nm, a broad peak in the range of 550–650 nm, and at 724 nm (Fig. S22). Here, the maximum was shifted from 621 nm to 602 nm due to the solvent effect. After subjecting the slurry to a temperature range of 263 to 303 K, a quenching in the luminescent signal was observed as the temperature was increased (Fig. S23). Moreover, the temperature sensitivity was calculated from the ratio of the intensities at 602 nm and 724 nm (*vide infra*).

Similar studies were conducted for **Eu@BTD**, where the emission peaks were recorded for the aqueous slurry at 298 K. The spectra showed two small peaks at 436 and 724 nm for the bands $^5D_1$(or higher) $\rightarrow {}^7F_0$ and $^5D_0 \rightarrow {}^7F_4$, respectively, and

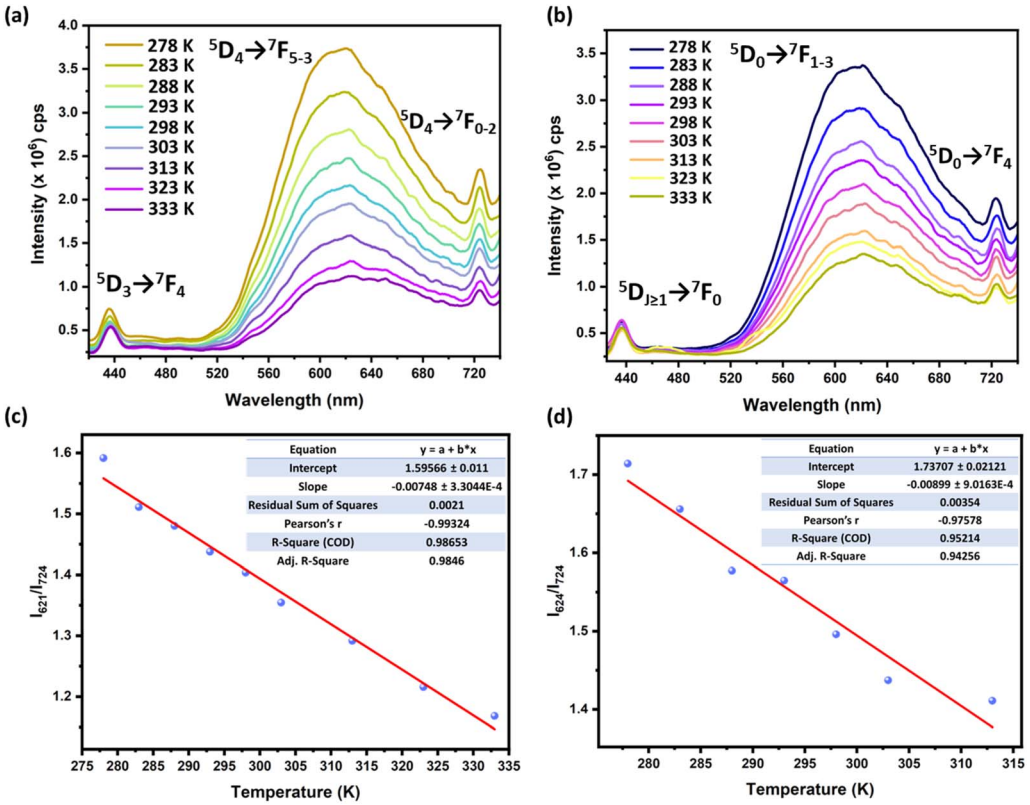

Fig. 4 Temperature-responsive behavior from 278 to 333 K in aqueous medium with a linear fit of thermometric parameter *vs.* temperature for (a and c) **Tb@BTD** and (b and d) **Eu@BTD**.

a broad peak in the 580–680 nm range for the $^5D_0 \rightarrow {}^7F_{1-3}$ band of Eu^{3+} and the $\pi^* \rightarrow \pi$ and/or $\pi \rightarrow$ n transition from **BTD**. In the methanolic slurry at 298 K, peaks at 429 nm, 550–650 nm and 724 nm were blue-shifted due to the solvent effect (Fig. S24).[47] In both cases, a quenching effect was seen when the temperature was elevated from 278 to 333 K in water (Fig. 4b) and from 258 to 313 K in methanol (Fig. S25). The thermal sensitivity of the **Eu@BTD** sensor was obtained using I_{621}/I_{724} for the aqueous mode and I_{604}/I_{724} for the methanol mode (*vide infra*). A possible explanation for the quenched emission for both **Tb@BTD** and **Eu@BTD** is the dissipated energies of the excited molecules in various pathways. In **Ln@BTD**, the emitting orbitals ($^5D_4$ for Tb^{3+} and $^5D_0$ for Eu^{3+}) lie close to the molecular orbitals of the organic luminophores in **BTD**. When the temperature is increased, the possibility of electronic transitions from $^5D_4$ or $^5D_0$ to the nearby orbitals of **BTD** is also increased, which, in turn, dissipates the energy.[49]

Calculation of sensitivity parameters. An essential parameter to determine the response of a sensor due to a variation of temperature is its thermal sensitivity (S_a). It is defined as a quotient of change in PL intensity ratio for the change in temperature, which is calculated using the thermometric parameter (Δ). In aqueous medium, both I_{621}/I_{724} and I_{624}/I_{724} vary linearly as a function of temperature (eqn (1) and (2)) from 278 to 333 K with good correlation coefficients R^2 of 0.985 and 0.943 for **Tb@BTD** and **Eu@BTD**, respectively (Fig. 4c and d).

$$\Delta = 3.638 - 0.0075\ T \quad (1)$$

$$\Delta = 4.192 - 0.0089\ T \quad (2)$$

Furthermore, the absolute sensitivity (S_a) is calculated using eqn (3), which is found to be 0.0161 K^{-1} and 0.0134 K^{-1} for **Tb@BTD** and **Eu@BTD**, respectively.

$$S_a = \left|\frac{\delta\Delta}{\delta T}\right| \quad (3)$$

Besides aqueous medium, similar calculations were performed to check the thermal sensitivity of both lanthanide-induced **BTD** compounds in methanol medium. The linear fit for I_{602}/I_{724} and I_{604}/I_{724} is done in eqn (4) and (5) for **Tb@BTD** and **Eu@BTD** with correlation coefficients R^2 of 0.937 and 0.981, respectively (Fig. S26 and S27).

$$\Delta = 7.353 - 0.0203\ T \quad (4)$$

$$\Delta = 6.143 - 0.015\ T \quad (5)$$

Using eqn (3), the absolute sensitivity of **Tb@BTD** and **Eu@BTD** in methanol is calculated to be 0.0357 K^{-1} and 0.0319 K^{-1}, respectively.

Another vital parameter that directly and quantitatively compares the thermal sensing efficiency with other sensors is relative sensitivity (S_r). S_r is defined as the relative change in

thermometric parameter (Δ) per degree change in temperature and is calculated by using eqn (6).

$$S_r = \frac{1}{\Delta}\left|\frac{\delta\Delta}{\delta T}\right| \times 100\% \quad (6)$$

The relative sensitivity in aqueous medium is calculated to be 1.033% K^{-1} and 0.813% K^{-1} at 278 K, and 1.404% K^{-1} and 1.118% K^{-1} at 333 K for **Tb@BTD** and **Eu@BTD**, respectively. Similarly, in methanolic medium, the values are found to be 0.816% K^{-1} at 263 K and 2.73% K^{-1} at 303 K for the **Tb@BTD** polymer. For **Eu@BTD**, S_r is 1.40% K^{-1} at 258 K and 2.29% K^{-1} at 313 K in methanolic medium. The results show that both frameworks are highly sensitive at elevated temperatures. However, the thermal sensitivity of **Tb@BTD** is higher in both the aqueous as well as methanolic media. Moreover, there is very little difference in the emissive properties of **Tb@BTD** and **Eu@BTD** in both media after thermal sensing from the low to high temperature (Fig. S28).

A noteworthy test was conducted to check the leaching of lanthanide ions from the framework during temperature sensing experiments. For this, the Ln-induced framework was filtered out of the aqueous slurry and the filtrate was irradiated at 380 nm. No notable emission was observed in the filtrate solution, indicating no leaching out of Tb^{3+}/Eu^{3+} into the solution (Fig. S29a). The digital images of the cuvette with **Ln@BTD** and the filtrate under UV and visible light are shown in Fig. S29b and S29c.

From the literature survey, there are only a handful of organic frameworks that have been exploited for ratiometric thermosensor studies, most of which work in the solid state (Table S3).[50–53] Recently, Kaczmarek *et al.* reported Dy, Eu and Tb induced TpBpy COFs exhibiting thermal sensitivity of 0.94% K^{-1} (at 280 K) for Dy loading and 1.403% K^{-1} (at 160 K) for 80 : 20 Eu : Tb_acac loading in TpBpy COF.[51] The sensitivity of Eu/Tb_acac@TpBpy COF decreases by varying the Ln ion content. Furthermore, TTA-DFP@Cu COF loaded with Eu or Tb shows a sensitivity of 2.4% K^{-1} (at 49.85 °C).[51] Another **Ln@COF** reported by Voort and co-workers displays temperature sensing properties in aqueous medium with relative sensitivity of 2.7% K^{-1} (at 283.15 K) when the Eu : Tb ratio is 3 : 97 in Bipy.[52] This is the maximum sensitivity reported for thermal parameters to date. However, the sensitivity of Bipy reduces to 2.3% K^{-1} (at 240 K) in the solid state. Moreover, Dy^{3+} and Eu^{3+}/Tb^{3+} (5 : 95) doped Bipy COF senses temperature by 2.42% K^{-1} (at 260 K) and 2.52% K^{-1} (at 210 K), respectively, in the solid state.[50] Also, Hencke and co-workers established a sensitivity of 1.66% K^{-1} (at 300 K) for $NaYF_4$: Eu,Yb/COF-300.[53] All the above-mentioned values are lower than or comparable to the relative sensitivity found for **Tb@BTD** and **Eu@BTD** in this work.

Detection in the physiological temperature range. There is a dire need for thermosensors that function in the physiological temperature range from 308 to 320 K for a number of biomedical applications. For instance, the thermal detection of brain tumor cells can be achieved because their temperature difference is in the 273.65–306.15 K range as compared to the nearby tissues. Therefore, the incentive to obtain such thermosensors is there. For this study, a homogeneous aqueous slurry of **Eu@BTD** was subjected to the physiological temperature range and its effect on the luminescence was studied. The spectral data reveal a quenching of 22% in the 580–680 nm ($^5D_0 \rightarrow {}^7F_{1-3}$) merged band, showing evident detection of thermal behaviour from the surroundings (Fig. S30 and S31).

Conclusions

In this contribution, a unique, timesaving technique for the synthesis of a hydrazone-linked COF was achieved. This streamlines the solvothermal method that uses long reaction time and a harsh reaction environment to attain periodicity in the frameworks. The prompt crystallization of a new hydrazone-connected COF, *viz.* **BTD**, was attained within 1.5 h, thus overcoming the limitations of tedious reaction methods. The crucial role of interlayer and intralayer H-bonding and π–π stacking to lock the highly flexible linkages was explained using high-level crystallographic simulations. This success in rapid crystallization of COF helps to build an understanding toward the cautious choice of monomers. Moreover, a rare property-function relationship was exploited for its colorimetric and luminescent behaviour by testing the framework as a wide-ranging H^+ donor and scavenger. In aqueous media, the highest luminescence was recorded at pH 4 because protonation of functionalities resulted in restricted intramolecular rotations (RIR). However, at basic pH, the luminescence is quenched due to the complete deprotonation of the framework. The detection of protons was also confirmed with the naked eye by colorimetric changes under both UV and visible light. The framework shows reversible behaviour toward pH sensitivity and its reusability was tested in ten consecutive cycles. More importantly, the functionalized linkage-bound trivalent lanthanides exhibited excellent thermal detection properties in two different polar protic media (water and methanol). A quenching effect was seen with an increase in temperature to a fairly high value. This makes the frameworks ideal candidates for use in biological systems as a dual proton donor and scavenger and an efficient thermal sensor.

Conflicts of interest

There are no conflicts to declare.

Data availability

Data for this work are presented in the manuscript and its supplementary information file (SI). Supplementary information: details of materials and physical measurements, experimental procedures and characterization using FTIR, TGA, NMR, FESEM, XRD, XPS, and gas sorption studies; curves for luminescence studies. See DOI: https://doi.org/10.1039/d5ta06543g.

Acknowledgements

H. B. acknowledges UGC, India, for the senior research fellowship. Authors acknowledge IISER Mohali for funding. Research

facilities (SAXS/WAXS, NMR, TEM and FESEM) at IISER Mohali are also acknowledged.

References

1 O. M. Yaghi, M. O'Keeffe, N. W. Ockwig, H. K. Chae, M. Eddaoudi and J. Kim, *Nature*, 2003, **423**, 705–714.
2 K. Geng, T. He, R. Liu, S. Dalapati, K. T. Tan, Z. Li, S. Tao, Y. Gong, Q. Jiang and D. Jiang, *Chem. Rev.*, 2020, **120**, 8814–8933.
3 H. Bhambri, S. Khullar, Sakshi and S. K. Mandal, *Mater. Adv.*, 2022, **3**, 19–124.
4 F. Haase and B. V. Lotsch, *Chem. Soc. Rev.*, 2020, **49**, 8469–8500.
5 X. Li, P. Yadav and K. P. Loh, *Chem. Soc. Rev.*, 2020, **49**, 4835–4866.
6 C. Feriante, A. M. Evans, S. Jhulki, I. Castano, M. J. Strauss, S. Barlow, W. R. Dichtel and S. R. Marder, *J. Am. Chem. Soc.*, 2020, **142**, 18637–18644.
7 H. Li, A. M. Evans, I. Castano, M. J. Strauss, W. R. Dichtel and J.-L. Bredas, *J. Am. Chem. Soc.*, 2020, **142**, 1367–1374.
8 S. Wang, A. D. Chavez, S. Thomas, H. Li, N. C. Flanders, C. Sun, M. J. Strauss, L. X. Chen, A. J. Markvoort, J.-L. Bredas and W. R. Dichtel, *Chem. Mater.*, 2019, **31**, 7104–7111.
9 P. Das and S. K. Mandal, *ACS Appl. Mater. Interfaces*, 2021, **13**, 14160–14168.
10 Y. Li, J. Sui, L.-S. Cui and H.-L. Jiang, *J. Am. Chem. Soc.*, 2023, **145**, 1359–1366.
11 A. M. Elewa, A. F. M. El-Mahdy, A. E. Hassan, Z. Wen, J. Jayakumar, T.-L. Lee, L.-Y. Ting, I. M. A. Mekhemer, T.-F. Huang, M. H. Elsayed, C.-L. Chang, W.-C. Lin and H.-H. Chou, *J. Mater. Chem. A*, 2022, **10**, 12378–12390.
12 Y. Zhao, H. Liu, C. Wu, Z. Zhang, Q. Pan, F. Hu, R. Wang, P. Li, X. Huang and Z. Li, *Angew. Chem., Int. Ed.*, 2019, **58**, 5376–5381.
13 Q. Fang, J. Wang, S. Gu, R. B. Kaspar, Z. Zhuang, J. Zheng, H. Guo, S. Qiu and Y. Yan, *J. Am. Chem. Soc.*, 2015, **137**, 8352–8355.
14 H. Bhambri and S. K. Mandal, *J. Chem. Phys.*, 2024, **160**, 054706.
15 J. Hu, Z. Huang and Y. Liu, *Angew. Chem., Int. Ed.*, 2023, **62**, e202306999.
16 H. L. Nyugen, C. Gropp and O. M. Yaghi, *J. Am. Chem. Soc.*, 2020, **142**, 2771–2776.
17 E. Jin, M. Asada, Q. Xu, S. Dalapati, M. A. Addicoat, M. A. Brady, H. Xu, T. Nakamura, T. Heine, Q. Chen and D. Jiang, *Science*, 2017, **357**, 673–676.
18 X. Li, J. Qiao, S. W. Chee, H.-S. Xu, X. Zhao, H. S. Choi, W. Yu, S. Y. Quek, U. Mirsaidov and K. P. Loh, *J. Am. Chem. Soc.*, 2020, **142**, 4932–4943.
19 G. Chen, H.-H. Lan, S.-L. Cai, B. Sun, X.-L. Li, Z.-H. He, S.-R. Zheng, J. Fan, Y. Liu and W.-G. Zhang, *ACS Appl. Mater. Interfaces*, 2019, **11**, 12830–12837.
20 A. Halder, S. Karak, M. Addicoat, S. Bera, A. Chakraborty, S. H. Kunjattu, P. Pachfule, T. Heine and R. Banerjee, *Angew. Chem., Int. Ed.*, 2018, **57**, 5797–5802.
21 X. Li, Q. Gao, J. Wang, Y. Chen, Z.-H. Chen, H.-S. Xu, W. Tang, K. Leng, G.-H. Ning, J. Wu, Q.-H. Xu, S. Y. Quek, Y. Lu and K. P. Loh, *Nat. Commun.*, 2018, **9**, 2335.
22 C. D. S. Brites, R. Marin, M. Suta, A. N. C. Neto, E. Ximendes, D. Jaque and L. D. Carlos, *Adv. Mater.*, 2023, **35**, 2302749.
23 A. Steinegger, O. S. Wolfbeis and S. M. Borisov, *Chem. Rev.*, 2020, **120**, 12357–12489.
24 C. D. S. Brites, P. P. Lima, N. J. O. Sitva, A. Millán, V. S. Amaral, F. Palacio and L. D. Carlos, *Nanoscale*, 2012, **4**, 4799–4829.
25 M. D. Dramićanin, *Methods Appl. Fluoresc.*, 2016, **4**, 042001.
26 B. Bendel and M. Suta, *J. Mater. Chem. C*, 2022, **10**, 13805–13814.
27 X. Wu, X. Zhang, Y. Li, B. Wang, Y. Li and L. Chen, *J. Mater. Sci.*, 2021, **56**, 2717–2724.
28 L. Chen, L. He, F. Ma, W. Liu, Y. Wang, M. A. Silver, L. Chen, L. Zhu, D. Gui, J. Diwu, Z. Chai and S. Wang, *ACS Appl. Mater. Interfaces*, 2018, **10**, 15364–15368.
29 M. C. Davis, *Synth. Commun.*, 2007, **37**, 1457–1462.
30 J. H. Chong, M. Sauer, B. O. Patrick and M. J. MacLachlan, *Org. Lett.*, 2003, **5**, 3823–3826.
31 *Dassault Systèmes BIOVIA. ViewerLite 5.0; Dassault Systèmes*, San Diego, 2002.
32 P. Das and S. K. Mandal, *ACS Appl. Mater. Interfaces*, 2021, **13**, 14160–14168.
33 M. Thommes, K. Kaneko, A. V. Neimark, J. P. Olivier, F. Rodriguez-Reinoso, J. Rouquerol and K. S. W. Sing, *Pure Appl. Chem.*, 2015, **87**, 1051.
34 X. Wang, L. Yue, P. Zhou, L. Fan and Y. He, *Inorg. Chem.*, 2021, **60**, 17249–17257.
35 P. Zhou, L. Yue, X. Wang, L. Fan, D.-L. Chen and Y. He, *ACS Appl. Mater. Interfaces*, 2021, **13**, 54059–54068.
36 G. A. Tompsett, L. Krogh, D. W. Griffin and W. C. Conner, *Langmuir*, 2005, **21**, 8214–8225.
37 Y. Li, J. Sui, L.-S. Cui and H.-L. Jiang, *J. Am. Chem. Soc.*, 2023, **145**, 1359–1366.
38 S.-Y. Zhang, X.-H. Tang, Y.-L. Yan, S.-Q. Li, S. Zheng, J. Fan, X. Li, W.-G. Zhang and S. Cai, *ACS Macro Lett.*, 2021, **10**, 1590–1596.
39 S.-L. Zhang, Z.-C. Guo, K. Xu, Z. Li and G. Li, *ACS Appl. Mater. Interfaces*, 2023, **15**, 33148–33158.
40 H. Wan, M. Li, L. Wang and Y. Song, *J. Mater. Chem. A*, 2023, **11**, 23829–23836.
41 Y. Li, C. Wang, S. Ma, H. Zhang, J. Ou, Y. Wei and M. Ye, *ACS Appl. Mater. Interfaces*, 2019, **11**, 11706–11714.
42 M. J. Frisch, G. W. Trucks, H. B. Schlegel, G. E. Scuseria, M. A. Robb, J. R. Cheeseman, G. Scalmani, V. Barone, B. Mennucci, G. A. Petersson, H. Nakatsuji, M. Caricato, X. Li, H. P. Hratchian, A. F. Izmaylov, J. Bloino, G. Zheng, J. L. Sonnenberg, M. Hada, M. Ehara, K. Toyota, R. Fukuda, J. Hasegawa, M. Ishida, T. Nakajima, Y. Honda, O. Kitao, H. Nakai, T. Vreven, J. A. Jr. Montgomery, J. E. Peralta, F. Ogliaro, M. Bearpark, J. J. Heyd, E. Brothers, K. N. Kudin, V. N. Staroverov, T. Keith, R. Kobayashi, J. Normand, K. Raghavachari, A. Rendell, J. C. Burant, S. S. Iyengar, J. Tomasi, M. Cossi, N. Rega, J. M. Millam, M. Klene, J. E. Knox, J. B. Cross, V. Bakken,

C. Adamo, J. Jaramillo, R. Gomperts, R. E. Stratmann, O. Yazyev, A. J. Austin, R. Cammi, C. Pomelli, J. W. Ochterski, R. L. Martin, K. Morokuma, V. G. Zakrzewski, G. A. Voth, P. Salvador, J. J. Dannenberg, S. Dapprich, A. D. Daniels, O. Farkas, J. B. Foresman, J. V. Ortiz, J. Cioslowski and D. J. Fox, *Gaussian 09*, Gaussian, Inc., Wallingford, CT, 2010.

43 M. Y. Berezin and S. Achilefu, *Chem. Rev.*, 2020, **110**, 2641–2684.

44 Y. Zhang, X. Shen, X. Feng, H. Xia, Y. Mu and X. Liu, *Chem. Commun.*, 2016, **52**, 11088–11091.

45 J.-Y. Yue, L.-P. Song, X.-L. Ding, Y.-T. Wang, P. Yang, Y. Ma and B. Tang, *Anal. Chem.*, 2022, **94**, 11062–11069.

46 X. Fang, Y. Liu, W.-K. Han, X. Yan, Y.-X. Shi, L.-H. Chen, Y. Jiang, J. Zhang and Z.-G. Gu, *Dyes Pigm.*, 2022, **205**, 110507.

47 Z. Smara, Y. Cheroura, D. Boyer, A. Boyer, A. Chafa, O. Ziane and R. Mahiou, *Optical Mater.*, 2020, **104**, 109932.

48 K. R. Murphy, *Appl. Spect.*, 2011, **65**, 233–236.

49 D. Zhao, X. Rao, J. Yu, Y. Cui, Y. Yang and G. Qian, *Inorg. Chem.*, 2015, **54**, 11193–11199.

50 A. M. Kaczmarek, Y.-Y. Liu, M. K. Kaczmarek, H. Liu, F. Artizzu, L. D. Carlos and P. V. D. Voort, *Angew. Chem., Int. Ed.*, 2020, **59**, 1932–1940.

51 A. M. Kaczmarek, H. S. Jena, C. Krishnaraj, H. Rijckaert, S. K. P. Veerapandian, A. Meijerink and P. V. D. Voort, *Angew. Chem., Int. Ed.*, 2021, **60**, 3727–3736.

52 P. G. Derakhshandeh, S. Abednatanzi, L. Bourda, S. Dalapati, M. Meledina, Y.-Y. Liu, A. G. Skirtach, K. V. Hecke, A. M. Kaczmarek and P. V. D. Voort, *J. Mater. Chem. C*, 2021, **9**, 6436–6444.

53 L. Bourda, A. M. Kaczmarek, M. Peng, S. Mohanty, H. Rijckaert, P. V. D. Voort and K. V. Hecke, *ACS Appl. Mater. Interfaces*, 2023, **15**, 37696–37705.